remote sensing

MDPI

Article

Post-Disturbance Forest Recovery in Wuyishan National Park: Spatiotemporal Heterogeneity, Recovery Timing, and Landscape Context

Hualiang Liu [1], Feizhou Zhang [2], Haowei Mu [3], Yefeng Xie [4] and Lifu Zhang [5,6,*]

[1] Hunan Provincial Key Laboratory for Big Data Smart Application of Natural Disaster Risks Survey of Highway Engineering, Changsha University, Changsha 410022, China
[2] Institute of Remote Sensing and Geographic Information Systems, Peking University, Beijing 100871, China
[3] College of Economics and Management, Northwest A&F University, Yangling, Shaanxi 712100, China
[4] College of National Park and Tourism, Central South University of Forestry & Technology, Changsha 410004, China
[5] Aerospace Information Research Institute, Chinese Academy of Sciences, Beijing 100101, China
[6] University of Chinese Academy of Sciences, Beijing 100049, China
* Correspondence: zhanglf@aircas.ac.cn

Highlights

What are the main findings?

- Five-year spectral recovery was spatially heterogeneous and generally higher after 2015; the median time to recover 80% of the initial disturbance-induced spectral loss was 9 years.
- Statistical associations with recovery did not always translate into improved prediction across disturbance patches.

What are the implications of the main findings?

- Combining disturbance mapping with recovery trajectories provides a more complete picture of forest dynamics in protected areas.
- Recovery timing and spatial heterogeneity can help identify areas requiring continued monitoring and field assessment.

Abstract

Protected-area monitoring has focused primarily on forest disturbance, while the subsequent recovery dynamics remain less well characterized. We assessed post-disturbance forest recovery in Wuyishan National Park, China, using Landsat time series spanning 1990–2025. Disturbances were mapped using LandTrendr and Random Forest classification. An adaptive spectral-variable selection approach was used to quantify five-year recovery and recovery timing, with timing estimates evaluated against visual interpretations of randomly sampled disturbed pixels. Generalized additive mixed models (GAMMs) examined associations between five-year recovery and disturbance, patch, terrain, landscape, and climate variables, while patch-grouped cross-validation assessed their incremental predictive contributions. Recovery was spatially heterogeneous, with a median five-year recovery index (RI5) of 0.627. Within a five-year window, 29.5% of the disturbed pixels recovered at least 80% of their initial disturbance-induced spectral loss. Kaplan–Meier analysis accounting for right censoring estimated a median of 9 years to first attainment of the 80% recovery threshold. Visual interpretations agreed with adaptive-model timing within ±3 years in 87.2% of comparisons. Annual median RI5 showed

Academic Editor: Nikolay S. Strigul

Received: 29 September 2026
Revised: 17 November 2026
Accepted: 25 November 2026
Published: 27 November 2026

Copyright: © 2026 by the authors. Licensee MDPI, Basel, Switzerland. This article is an open access article distributed under the terms and conditions of the Creative Commons Attribution (CC BY) license.

a marked upward level shift from 2016 onward, which persisted after covariate matching. Lower RI5 was associated with longer disturbance duration, intermediate-sized patches, and proximity to rivers. Patch characteristics and terrain improved out-of-patch prediction, whereas additional contributions from landscape context and climate were not statistically distinguishable from zero (out-of-patch $R^2 = 0.088$). These findings complement disturbance mapping by quantifying recovery magnitude and timing and evaluating which characteristics contribute to explaining and predicting recovery variation across disturbance patches.

Keywords: Landsat time series; LandTrendr; post-disturbance recovery; recovery timing; protected-area monitoring; Wuyishan National Park

1. Introduction

Protected areas are a central component of global biodiversity conservation and help reduce habitat loss and other anthropogenic pressures on ecosystems [1–3]. Protected status, however, does not isolate ecosystems from natural disturbances, climatic stress, or human activities. Remote sensing has become an important component of protected-area monitoring by enabling repeated assessment of habitat condition, disturbance, and landscape change over large areas [4,5]. In forested protected areas, disturbance effects can persist beyond the initial loss or degradation of vegetation, and their longer-term consequences depend on how affected forests recover [6,7]. Examining recovery therefore extends disturbance monitoring from identifying forest change to assessing its persistence and subsequent trajectory. Forests experiencing similar levels of disturbance may subsequently follow different recovery trajectories, making these differences relevant to the long-term monitoring and management of protected forests.

Long-term satellite time series enable post-disturbance forest recovery to be assessed across broad spatial extents and multi-decadal periods. The opening of the Landsat archive and advances in time-series analysis have enabled forest change to be represented as trajectories encompassing both disturbance and subsequent regrowth, rather than as isolated changes between image dates [8–12].-Within these trajectories, a five-year window provides a commonly used operational interval for characterizing short-term spectral regrowth, while time-to-threshold metrics capture longer-term recovery timing. Kennedy et al. [13] introduced the Recovery Indicator (RI), scaling the five-year post-disturbance Normalized Burn Ratio (NBR) gain by the initial spectral loss to quantify relative short-term regrowth. White et al. [14] extended this approach to a nationwide assessment of Canadian forests by pairing five-year relative NBR recovery with years to recovery (Y2R), defined as the time required to regain 80% of the pre-disturbance value. Combining five-year recovery magnitude with time to 80% attainment has been applied in large-scale assessments of post-harvest regeneration [15]. Related studies have compared post-disturbance forest recovery across management regimes using structural indicators [16] and mapped and validated spatiotemporal recovery trends using time-to-threshold metrics [17]. Other Landsat trajectory metrics have also been used to characterize short-term post-fire vegetation return [18].

Post-disturbance recovery is nevertheless multidimensional and strongly context dependent. Recovery varies with disturbance severity and patch size, climatic conditions, topography, and landscape setting, indicating that post-disturbance trajectories reflect both disturbance history and environmental context [6,7,18,19]. Spectral recovery also represents only one dimension of forest recovery. Studies have compared Landsat-derived spectral recovery with LiDAR-derived canopy height and cover [20], while spectral-

unmixing approaches have used tree-cover and bare-ground fractions as alternative recovery indicators [21]. These studies underscore that recovery estimates depend on the forest attributes represented by the selected indicators, and that a return toward pre-disturbance spectral conditions does not necessarily imply complete recovery of forest structure or ecological function. Studies in China report similar heterogeneity. Climate and topography are associated with short-term recovery in plantation forests of southern China, while disturbance type, severity, climate, and elevation differentiate recovery patterns in boreal forests of Northeast China [22,23].

Despite progress in forest-recovery research, post-disturbance recovery has received less attention than disturbance detection in remote-sensing studies of protected areas. A systematic review of 105 studies published between 2015 and 2025 found that 98 addressed disturbance detection, whereas 45 examined recovery detection and 23 included recovery modeling [24]. Recent work in Amazonian protected areas has used multi-source remote sensing to distinguish natural post-fire recovery from persistent post-disturbance conversion [25]. Nevertheless, the magnitude, timing, and spatial heterogeneity of subsequent recovery, as well as their relationships with disturbance characteristics and landscape context, remain less well characterized in protected areas.

Wuyishan National Park protects a representative mid-subtropical evergreen broadleaved forest ecosystem in southeastern China [26]. Its forest landscape has been shaped by long-standing interactions between conservation and human land use [27,28]. The national park pilot initiated in 2015 marked a transition toward more integrated governance and strengthened conservation management, creating a temporal context for examining disturbance–recovery dynamics across this governance transition. Previous studies have examined vegetation change across protection levels [29] and long-term forest disturbance dynamics [28]. Using Landsat-derived enhanced vegetation index (EVI) time series and wild binary segmentation, Fan et al. [29] reported overall vegetation greening from 1986 to 2020, with more frequent abrupt EVI changes in less-protected areas. Liu et al. [28] used Landsat time series and the Landsat-based detection of trends in disturbance and recovery (LandTrendr) algorithm to reconstruct disturbance dynamics during 1991–2023. They estimated that approximately 6.0% of the park area experienced disturbance and reported that disturbance levels remained low after the 2015 national park pilot. However, their analysis focused on disturbance occurrence, extent, and drivers rather than quantifying the magnitude and timing of spectral recovery along individual post-disturbance trajectories.

This study examines post-disturbance forest recovery in Wuyishan National Park using a multi-decadal Landsat time series. Three questions guide the analysis: (1) How does post-disturbance recovery vary across space and time within the national park? (2) To what extent and over what time scales do disturbed forests recover? (3) Which factors are associated with recovery heterogeneity, and how much do different variable groups contribute to recovery prediction? We quantify five-year recovery using an adaptive spectral-variable selection approach and estimate time to first attainment of the 80% recovery threshold using survival analysis that accounts for right censoring. Recovery-time estimates are also evaluated against visual interpretations. Generalized additive mixed models (GAMMs) are used to examine recovery associations, while patch-grouped cross-validation assesses the predictive contributions of different variable groups. This study complements previous assessments of vegetation change and disturbance in Wuyishan by quantifying the magnitude and timing of spectral recovery and evaluating which measured characteristics help explain and predict recovery variation across disturbance patches.

2. Materials and Methods

2.1. Study Area and Data

Wuyishan National Park is located along the Fujian–Jiangxi provincial boundary in southeastern China and covers 1280 km² (Figure 1) [30]. The park protects representative mid-subtropical evergreen broad-leaved forest ecosystems and is one of the first five national parks established under China's national park system. The national park system represents a reform of China's protected-area governance, emphasizing the conservation of nationally representative ecosystems through integrated management and strengthened ecological protection [31,32]. Wuyishan was included in the national park system pilot initiated in 2015, which sought to integrate previously fragmented protected areas and establish unified management, resource supervision, and ecological conservation mechanisms [32,33]. The park was formally established in 2021 following the pilot period.

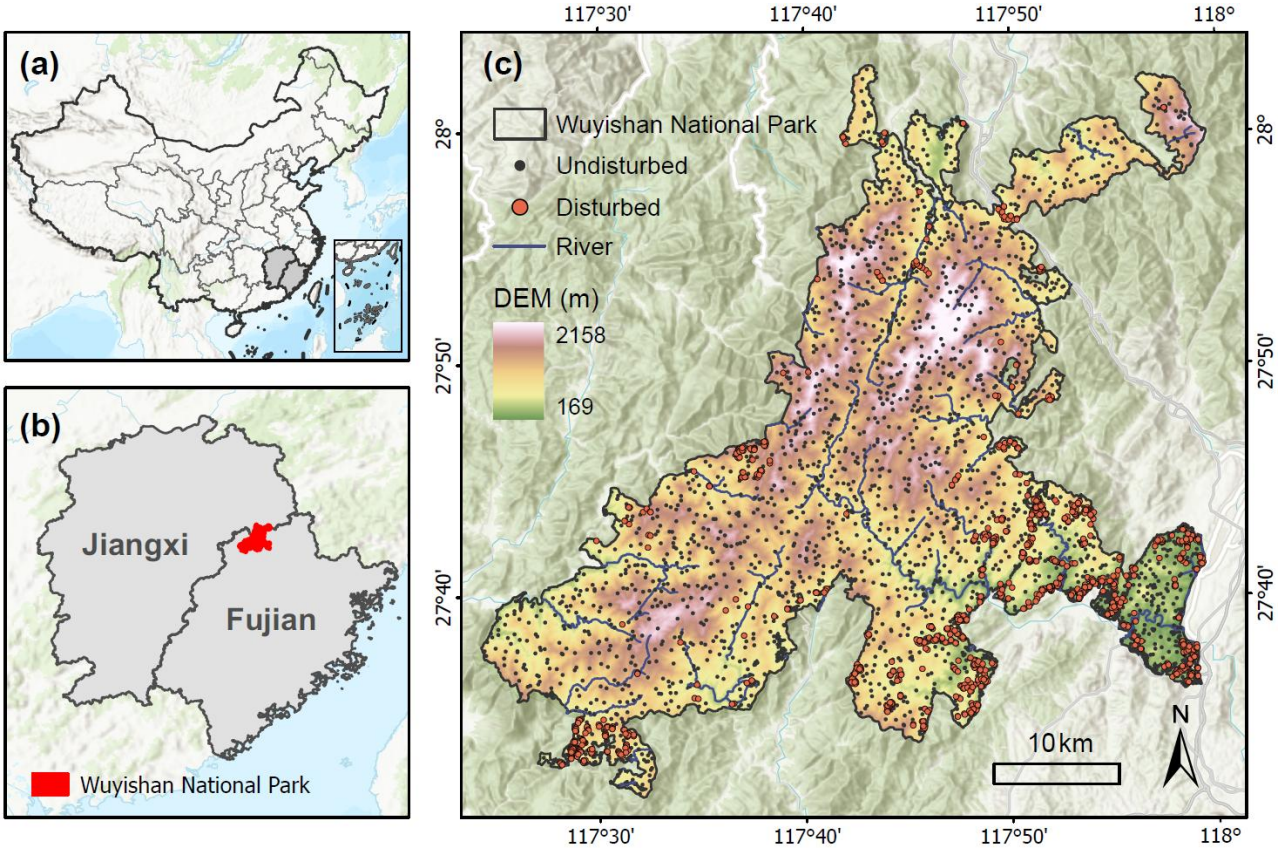


Figure 1. Location map of study area and distribution of reference samples. (**a**) location of Jiangxi and Fujian provinces in China; (**b**) location of Wuyishan National Park along the Jiangxi–Fujian provincial border; and (**c**) elevation (DEM), river network, and distribution of undisturbed and disturbed reference samples within Wuyishan National Park.

Landsat 5, 7, 8, and 9 Collection 2 Tier 1 Level-2 surface-reflectance imagery from 1990 to 2025 was accessed and processed in Google Earth Engine. The resulting Landsat time series was used for forest disturbance mapping and post-disturbance recovery analysis. Topographic context was characterized using SRTM elevation and DEM-derived slope. Road, river, and village vector data were obtained from OpenStreetMap (OSM). These ancillary datasets provided the topographic and landscape variables used in the recovery analysis.

Reference data for disturbance classification were developed from randomly generated candidate samples followed by visual verification. Candidate disturbance samples were drawn from the China Forest Disturbance Maps (1986–2020) produced by Liu et al.

[34], whereas candidate undisturbed samples were randomly generated within the national park. Given that the national disturbance product exhibited an overall accuracy of 0.96 but a disturbed-class user's accuracy of 0.76, all candidate samples were screened using the Landsat Time Series Viewer developed by the eMapR laboratory at Oregon State University. NBR trajectories and annual Landsat image chips were examined jointly to verify disturbance signals, identify disturbance years, and remove false detections or spectrally unstable undisturbed samples. This process yielded 1112 disturbed and 1964 undisturbed reference samples for Random Forest training and spatial validation (Figure 1). The disturbance reference years spanned 1991–2023, with 59.6% of samples from 1991 to 2000 and 3.7% during 2015–2023.

2.2. Methods

The methodological framework was organized around three related questions: where and when forest disturbances occurred, how post-disturbance spectral recovery varied in magnitude and timing, and how recovery was associated with disturbance characteristics and landscape context (Figure 2). Forest disturbances were first mapped from the Landsat time series using LandTrendr and Random Forest classification. Post-disturbance spectral trajectories were then used to quantify complementary measures of recovery magnitude and timing. Recovery magnitude was examined spatially and across disturbance years, while recovery timing was analyzed separately. Generalized additive mixed models examined the associations of five-year recovery with disturbance, patch, terrain, landscape, and climate variables, while patch-grouped cross-validation quantified their incremental predictive contributions. Sensitivity analyses assessed the robustness of recovery estimates and modeled relationships to key methodological choices.

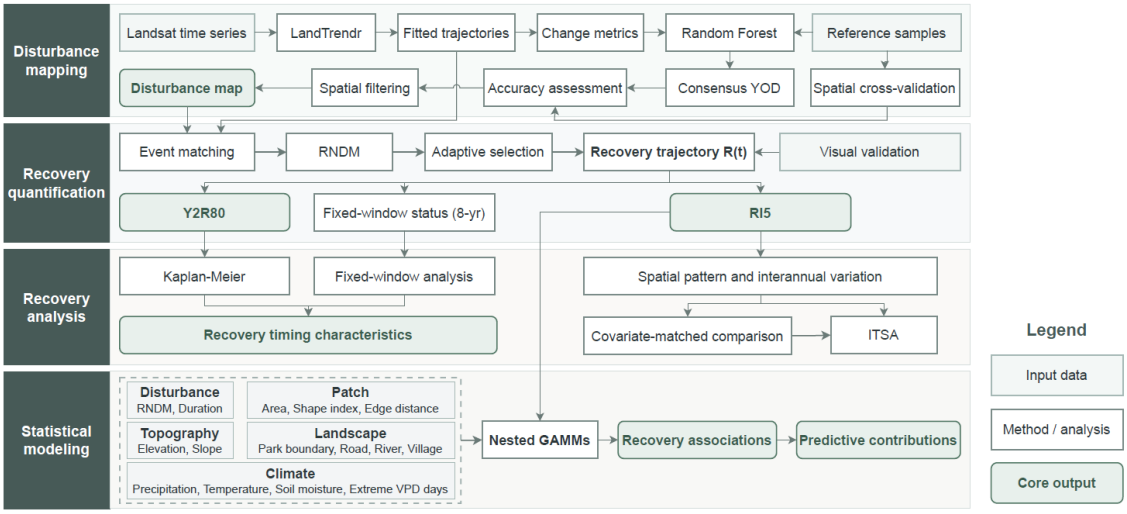


Figure 2. Methodological framework. Abbreviations: RNDM, relative normalized disturbance magnitude; RI5, five-year recovery index; R80, threshold for recovery of 80% of the disturbance-induced spectral loss; Y2R80, years to first R80 attainment; YOD, year of disturbance; GAMM, generalized additive mixed model; ITSA, interrupted time-series analysis.

2.2.1. Forest Disturbance Mapping

Annual Landsat surface-reflectance composites were constructed in Google Earth Engine for 1990–2025 using observations acquired between 15 May and 15 October. Clouds, cloud shadows, snow, and water were masked before compositing. Five spectral variables, Landsat B5, B7, Tasseled Cap Wetness (TCW), NBR, and Normalized Difference Fraction Index (NDFI), were used to characterize forest spectral change. LandTrendr was applied separately to each variable to fit annual spectral trajectories [8,35]. Disturbance

segments occurring between 1991 and 2024 were evaluated, and the segment representing the greatest vegetation loss was retained for each spectral variable. LandTrendr was run with a maximum of eight segments, a spike threshold of 0.9, a vertex-count overshoot of 3, a recovery threshold of 0.25, a *p*-value threshold of 0.05, a best-model proportion of 0.75, and a minimum of six valid observations; one-year recovery segments were not allowed.

Forest disturbance was identified using a binary Random Forest (RF) classifier. Five LandTrendr change attributes, disturbance magnitude (mag), duration (dur), pre-disturbance spectral value (preval), rate of change (rate), and disturbance-to-noise ratio (dsnr), were derived from each spectral variable, yielding 25 spectral-temporal predictors. The RF consisted of 500 trees with a maximum depth of 15. Reference samples were partitioned into 80 spatial blocks using weighted K-means clustering, and classification performance was evaluated using five-fold stratified group cross-validation. Overall accuracy, kappa coefficient, and disturbed-class user's and producer's accuracies were calculated from aggregated out-of-fold predictions, with confidence intervals estimated by spatial-block bootstrap resampling. All classification accuracy metrics were calculated from the RF predictions before spatial post-processing.

A consensus year of disturbance (YOD) was derived from the five variable-specific LandTrendr estimates for pixels classified as disturbed. The modal year was retained; in the case of ties, the candidate year minimizing the total absolute deviation from all valid variable-specific YODs was selected, with the earlier year used when a tie remained. Pixels with more than 50% of their area within the national park boundary were retained. Disturbed pixels without a valid YOD and spatially isolated pixels without an eight-neighbor disturbed pixel within ±3 years were removed. Single-pixel holes enclosed by disturbed pixels were filled using the modal YOD of neighboring disturbed pixels. Disturbance patches were delineated using eight-neighbor connectivity, with adjacent disturbed pixels assigned to the same patch when their YODs differed by no more than three years. Temporal accuracy of the consensus YOD was evaluated against the visually interpreted disturbance years of the disturbed reference samples.

2.2.2. Post-Disturbance Recovery Quantification

Post-disturbance recovery was quantified from LandTrendr-fitted trajectories using an adaptive spectral-variable approach. A spectral variable was selected separately for each disturbed pixel according to its normalized disturbance response, and subsequent recovery was measured relative to the disturbance-induced spectral change represented by the selected trajectory. This allowed differences in spectral sensitivity among variables to be accommodated while retaining a consistent basis for recovery assessment.

Relative normalized disturbance magnitude (RNDM) was used to select the spectral trajectory for subsequent recovery calculation. For each candidate spectral variable k, RNDM was calculated as follows:

$$RNDM_k = \frac{|B_k - D_k|}{S_k} \quad (1)$$

where B_k is the LandTrendr-fitted value one year before the variable-specific year of disturbance (YOD), D_k is the fitted value at the end of the corresponding disturbance segment, and S_k represents the spectral range of variable k. Candidate events were restricted to those with a YOD within ±3 years of the consensus YOD. To place disturbance responses from different spectral variables on a comparable scale, S_k was defined using a robust percentile range:

$$S_k = Q_{95,k} - Q_{5,k} \quad (2)$$

where $Q_{95,k}$ and $Q_{5,k}$ are the 95th and 5th percentiles of all valid annual raw values of variable k from the final disturbed-pixel population during 1990–2025. The spectral variable with the highest RNDM was retained for each pixel, together with its corresponding disturbance segment.

Post-disturbance recovery was calculated from the fitted trajectory of the selected spectral variable as follows:

$$R(t) = \frac{F(t) - D}{B - D} \quad (3)$$

where $F(t)$ is the fitted value at year t, and B and D are the pre-disturbance baseline and disturbance endpoint, respectively. Under this formulation, $R(t) = 0$ at the disturbance endpoint and $R(t) = 1$ when the fitted trajectory returns to the pre-disturbance baseline. Recovery values were not constrained to [0,1], allowing values below 0 or above 1 to be retained.

Five-year recovery magnitude was quantified using the five-year recovery index (RI5):

$$RI5 = R(t_e + 5) \quad (4)$$

where t_e is the disturbance endpoint year. RI5 represents the proportion of the initial disturbance-induced spectral loss recovered five years after the disturbance ended. This relative formulation follows established Landsat-based recovery metrics that scale post-disturbance spectral change by the magnitude of the preceding disturbance [13,14]. The five-year interval was used as a consistent window for quantifying short-term spectral regrowth, following previous Landsat-based assessments [13–16]. RI5 was calculated only where five complete post-disturbance years were available. An RI5 of 0.8 indicates recovery of 80% of the initial spectral loss, whereas RI5 = 1 indicates a return to the pre-disturbance spectral baseline.

2.2.3. Recovery Timing Analysis

Recovery timing was quantified as the number of years from the disturbance endpoint to the first attainment of 80% of the initial disturbance-induced spectral loss. R80 was defined as $R(t) \geq 0.8$, and Y2R80 as the number of complete post-disturbance years to first R80 attainment. The 80% criterion was used as an operational threshold for substantial spectral recovery. Similar thresholds have been applied in Landsat-based assessments of post-disturbance forest recovery and evaluated against airborne laser scanning measures of forest structure [20].

Available follow-up varied among disturbance events because all trajectories were observed through 2025. Pixels that attained R80 during the observation period were assigned the corresponding Y2R80, whereas those that had not attained R80 were treated as right-censored at their last complete post-disturbance year. Pixels without at least one complete post-disturbance year were excluded. The Kaplan–Meier estimator was used to account for right censoring and estimate the cumulative probability of first R80 attainment over time [36,37]. Cumulative attainment was expressed as 1-$S(t)$, where $S(t)$ is the probability that R80 has not yet been attained by time t. The median time to first R80 attainment was derived from the Kaplan–Meier estimate, with 95% confidence intervals obtained from 2000 bootstrap replicates using disturbance patches as the resampling units.

To provide a comparison under equal follow-up, R80 attainment was also summarized within a fixed 8-year observation window. The 8-year window provided a medium-term complement to RI5 and fell within the range of recovery times reported in previous Landsat-based studies [17,38]. Only pixels with at least eight complete post-disturbance years were included, and attainment was recorded according to whether R80 was first reached within this interval.

Recovery timing was visually assessed for 300 pixels randomly sampled from the disturbed pixels eligible for recovery-timing analysis. An interactive viewer displayed annual raw observations and LandTrendr-fitted trajectories for all five spectral variables. The visually interpreted year of sustained R80 attainment was determined from the overall trajectory and temporal consistency of annual observations, allowing for isolated anomalous values. Agreement with model-derived recovery timing was evaluated using a ±3-year tolerance, with one-sided R80 attainment treated as disagreement.

2.2.4. Statistical Modeling of Five-Year Recovery

To examine how five-year spectral recovery varied with disturbance characteristics and landscape context, RI5 was modeled using a generalized additive mixed model (GAMM). Fifteen explanatory variables were considered in five groups: disturbance characteristics (disturbance duration and RNDM), patch characteristics (patch area, patch shape index, and pixel distance to the disturbance-patch edge), terrain (elevation and slope), landscape context (distances to the park boundary, roads, rivers, and villages), and climate (five-year cumulative precipitation, mean temperature, mean soil moisture, and extreme vapor pressure deficit (VPD) days). RNDM was retained as an adjustment covariate representing normalized spectral disturbance magnitude. Patch shape index was calculated as $0.25P/\sqrt{A}$, where P and A are patch perimeter and area, respectively. The four climate variables were derived from ERA5-Land over the five years following the disturbance endpoint. Soil moisture was represented by mean volumetric soil water content in the second soil layer (7–28 cm). Extreme VPD days were defined as the number of days on which daily VPD exceeded the grid-cell-specific 95th-percentile threshold for the corresponding calendar month, calculated using the 1991–2020 baseline.

Explanatory-variable distributions, pairwise Spearman correlations, and variance inflation factors were examined before model fitting. Disturbance duration, patch area, and distances to the patch edge, park boundary, and rivers were transformed using log(1 + x). A Gaussian GAMM with an identity link was fitted using cubic regression splines and restricted maximum likelihood [39]. A random intercept for disturbance patch was included to account for the non-independence of pixels belonging to the same spatiotemporal disturbance patch. The smooth basis dimensions were set to k = 15 for RNDM, k = 6 for disturbance duration, and k = 10 for all remaining smooth terms.

Statistical support for smooth terms was assessed using approximate *F*-tests. Full-data model fit was summarized using conditional in-sample R^2 and RMSE derived from fitted values including the patch-level random effect. Adjusted relationships were represented by centered smooth partial effects with 95% confidence intervals and displayed over the 1st–99th percentile range of each explanatory variable. For descriptive comparison of modeled response amplitudes, the partial-effect range was calculated as the difference between the maximum and minimum centered smooth effects over this range.

Predictive performance was evaluated using five-fold cross-validation grouped by disturbance patch, with all pixels belonging to the same patch assigned to a single fold. Fold allocation was balanced by pixel count. Five nested GAMMs were constructed sequentially: M1 included disturbance characteristics; M2 additionally included patch characteristics; M3 added terrain variables; M4 added landscape-context variables; and M5 further incorporated climate variables. Because held-out patches were excluded from model fitting, their predictions were based on the population-level GAM component rather than patch-specific random intercepts. Predictive performance was assessed using pooled out-of-fold R^2 and RMSE. Changes in these metrics between successive models were quantified using 2000 paired patch-level bootstrap resamples of the out-of-fold predictions, retaining all pixels within each resampled patch and using the same resamples for both models in each comparison.

2.2.5. Sensitivity and Robustness Analyses

Sensitivity analyses examined whether the main recovery estimates and predictor–RI5 relationships depended on spectral-variable selection, recovery definition, or model specification. RI5 and eight-year R80 attainment were recalculated using B5, B7, TCW, NBR, and NDFI as fixed spectral variables. Recovery-time distributions were compared using Kaplan–Meier estimates for pixels with corresponding disturbance events and valid recovery-timing records across all five variables. Differences were evaluated using disturbance-patch-level bootstrap resampling. The adjusted relationship between RI5 and distance to patch edge was examined for the adaptive approach, NBR, TCW, and NDFI using reduced additive models fitted to their common-support sample. Recovery-timing sensitivity was assessed by repeating the time-to-attainment analysis for R70 and R90 in addition to the primary R80 threshold, using the same right-censoring and Kaplan–Meier procedures. Sensitivity of fixed-window R80 attainment to follow-up length was evaluated using 6- and 10-year windows in addition to the primary 8-year window.

The robustness of the GAMM relationships was further examined with respect to extreme RI5 values and residual spatial dependence. Smooth-response shapes were compared before and after excluding the upper and lower 0.5% of RI5 observations, with similarity quantified using Spearman rank correlations. Residual spatial dependence was evaluated at lag distances of 30, 60, 90, 150, and 300 m by comparing GAM-only residuals, which excluded the patch-level random intercept, with full conditional residuals that included it.

Because RNDM and RI5 both incorporate disturbance spectral amplitude, sensitivity to RNDM adjustment was evaluated using paired GAMMs fitted to the same observations. The two models used identical predictor transformations, random-effect structure, and spline basis dimensions, differing only in whether RNDM was included. Similarity between the resulting smooth relationships was evaluated using Spearman correlations together with changes in modeled partial-effect ranges and end-to-end contrasts.

3. Results

3.1. Spatial and Temporal Patterns of Five-Year Recovery

The Random Forest disturbance classifier achieved an overall accuracy of 95.5% (95% CI: 94.5–96.5%) and a kappa of 0.903 (95% CI: 0.879–0.923) under spatial cross-validation. User's and producer's accuracies for the disturbed class were 93.5% (95% CI: 90.1–95.9%) and 94.2% (95% CI: 92.2–96.0%), respectively. Temporal accuracy was assessed by comparing the consensus YOD with visually interpreted disturbance years from the disturbed reference samples. The assigned YOD agreed with the reference year within ±1 year for 90.96% of samples and within ±3 years for 95.04%, with a mean absolute error of 0.76 years (Figure 3).

From 1991 to 2024, mapped forest disturbance covered 3345.3 ha across 4463 disturbance patches. Post-disturbance recovery trajectories were identified for 37,091 pixels, of which 34,844 had sufficient follow-up for RI5 calculation. The remaining 2247 pixels corresponded to disturbance events ending after 2020 and therefore lacked the five post-disturbance years required for RI5 estimation by 2025. RI5 had a mean of 0.628, a median of 0.627, and an interquartile range of 0.402–0.846. Five years after disturbance, 29.5% of pixels had recovered at least 80% of the initial disturbance-induced spectral loss (RI5 ≥ 0.8), while 12.3% had returned to or exceeded the pre-disturbance spectral baseline (RI5 ≥ 1.0).

The spatial distribution of RI5 showed pronounced heterogeneity across the park (Figure 4). Disturbed pixels were relatively sparse over much of Wuyishan National Park but formed denser concentrations in several eastern, southeastern, and southwestern areas. The enlarged regions A–D showed that low and high RI5 values were spatially interspersed within local disturbance concentrations, indicating fine-scale variation in five-year recovery magnitude. No clear park-wide spatial gradient in RI5 was evident.

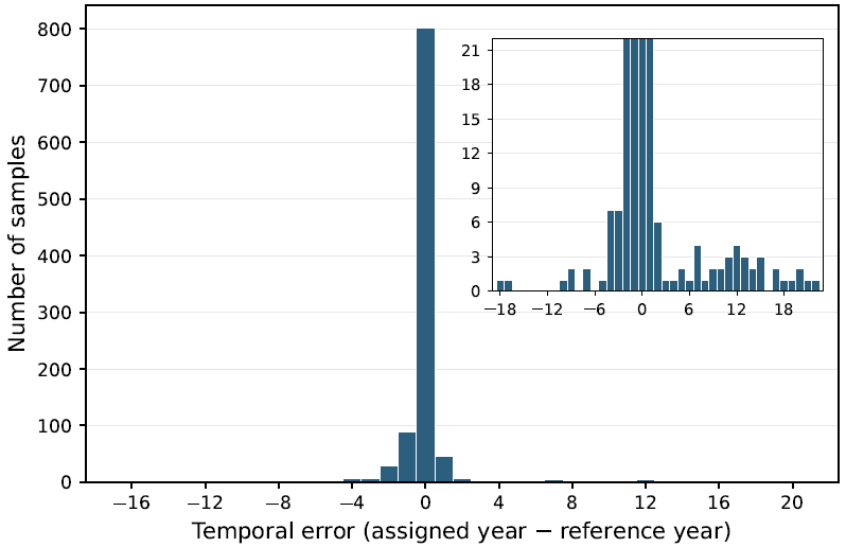


Figure 3. Distribution of temporal errors between the consensus year of disturbance (YOD) and visually interpreted reference years. Positive values indicate later assigned years. The inset plot provides a zoomed-in view (y-axis limited to 0–22) to illustrate the distribution of long-tail temporal errors.

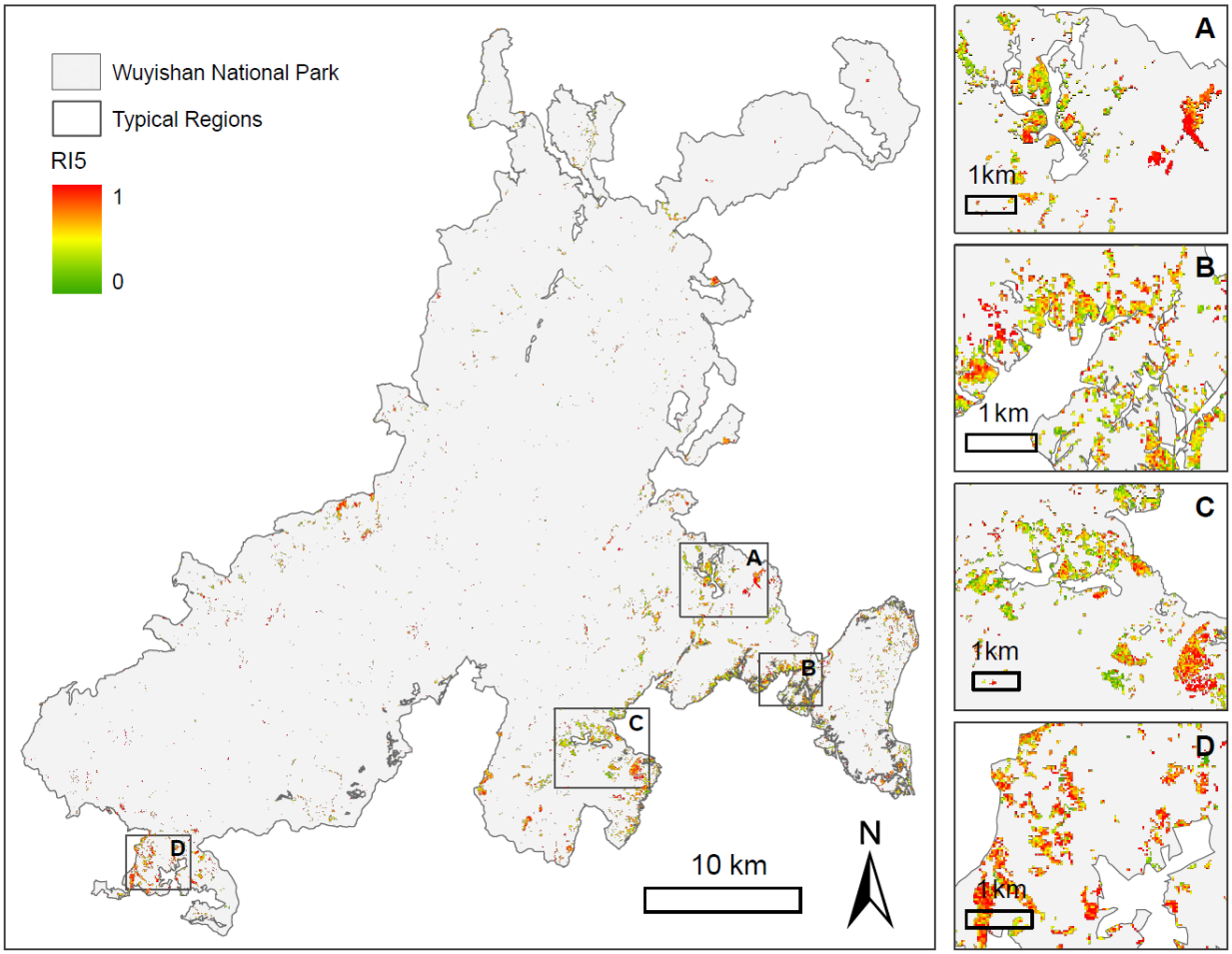


Figure 4. Spatial distribution of five-year spectral recovery (RI5) in Wuyishan National Park. Insets (**A**–**D**) enlarge representative areas with relatively dense disturbance concentrations. For visualization, RI5 values below 0 and above 1 are displayed at the lower and upper limits of the color scale, respectively.

Five-year recovery also varied across disturbance years (Figure 5). Annual median RI5 ranged from 0.497 in 2006 to 0.854 in 2016. Relatively low median RI5 values occurred in several years between 2005 and 2012, whereas disturbances occurring after 2015 generally exhibited higher five-year recovery levels. Median RI5 ranged from 0.770 to 0.854 during 2016–2020, compared with values mostly below 0.65 during 2005–2014, while substantially fewer disturbed pixels contributed to the annual distributions after 2015, as indicated by the box-fill colors.

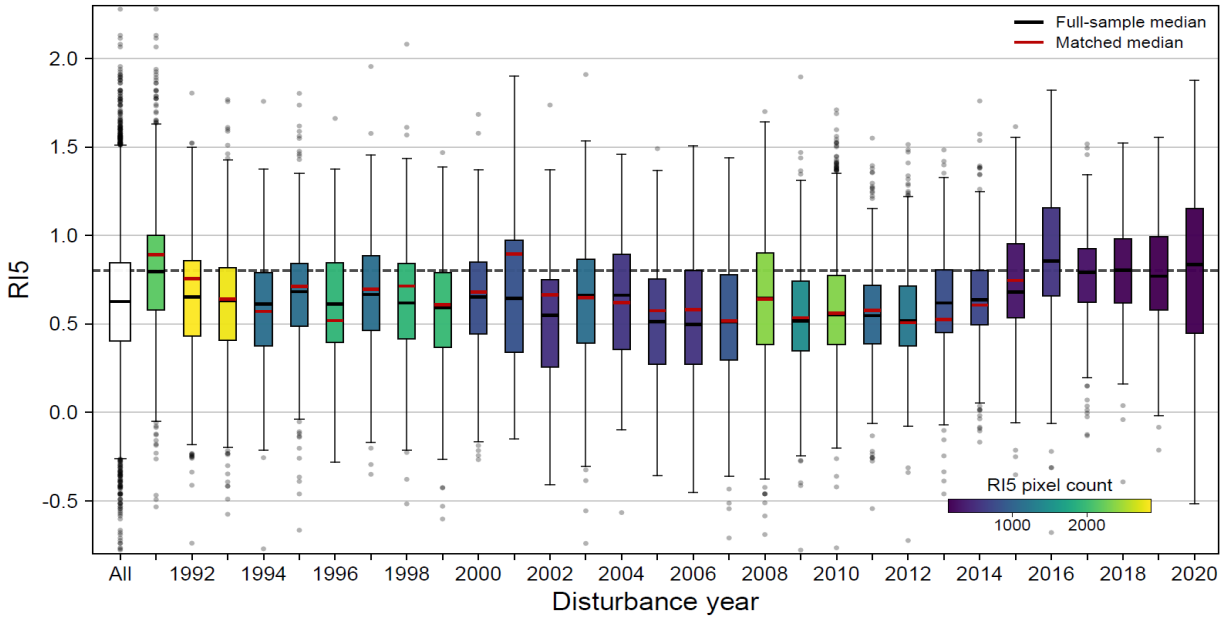


Figure 5. Distribution of RI5 by disturbance year from 1991 to 2020. The "All" box shows the pooled distribution. Boxes indicate interquartile ranges, center lines indicate full-sample medians, whiskers extend to 1.5 times the interquartile range, and points indicate observations beyond the whiskers. Red horizontal lines indicate matched medians of historical pixels for 1991–2015. The dashed line marks RI5 = 0.8, and fill color indicates the number of pixels with valid RI5 values in each year.

To examine whether this post-2015 recovery increase persisted after accounting for measured disturbance and landscape characteristics, we conducted a matching-based sensitivity analysis. Pixels with valid RI5 estimates from 2016 to 2020 were matched to historical pixels from 1991 to 2015 using 11 covariates describing disturbance characteristics, patch characteristics, terrain, and landscape context. Up to 10 historical pixels were retained for each post-2015 pixel. Of the 1352 post-2015 pixels, 1308 were matched to 5420 distinct historical pixels. Covariate balance was close after matching, with absolute standardized mean differences (SMDs) below 0.1 for 10 of the 11 covariates and a maximum of 0.124 for distance to roads. Comparison with the matched historical medians (red lines in Figure 5) continued to show generally higher RI5 for disturbances occurring during 2016–2020.

To further assess this temporal shift, interrupted time-series analysis (ITSA) was applied to annual median RI5 using the 2015 national park pilot as the intervention point. Statistical inference was based on Newey–West heteroskedasticity- and autocorrelation-consistent standard errors, and rolling ITSA was used to examine temporal variation in level- and trend-change statistics (Figure 6). The ITSA indicated a significant upward level shift in annual median RI5 following the pilot. The estimated level change was +0.269 (95% CI: 0.192–0.347, $p < 0.001$), whereas the trend change was negligible (−0.0014 yr^{-1}, $p = 0.884$). The pre-pilot trend was slightly negative but not statistically supported (−0.0044 yr^{-1}, $p = 0.072$). Thus, the higher RI5 observed from 2016 onward primarily reflected an upward shift in recovery level rather than a change in subsequent temporal trend. In the rolling

analysis, the positive level-change statistic increased toward 2015–2016 and was highest around the pilot transition, while the trend-change statistic approached zero by 2016 (Figure 6b). Applying the same ITSA specification to the matched annual RI5 medians yielded a similar level change (+0.269, 95% CI: 0.181–0.357), compared with the original estimate. The matched-series trend change was small and not statistically significant (+0.004 yr^{-1}, 95% CI: −0.011 to 0.019; $p = 0.609$).

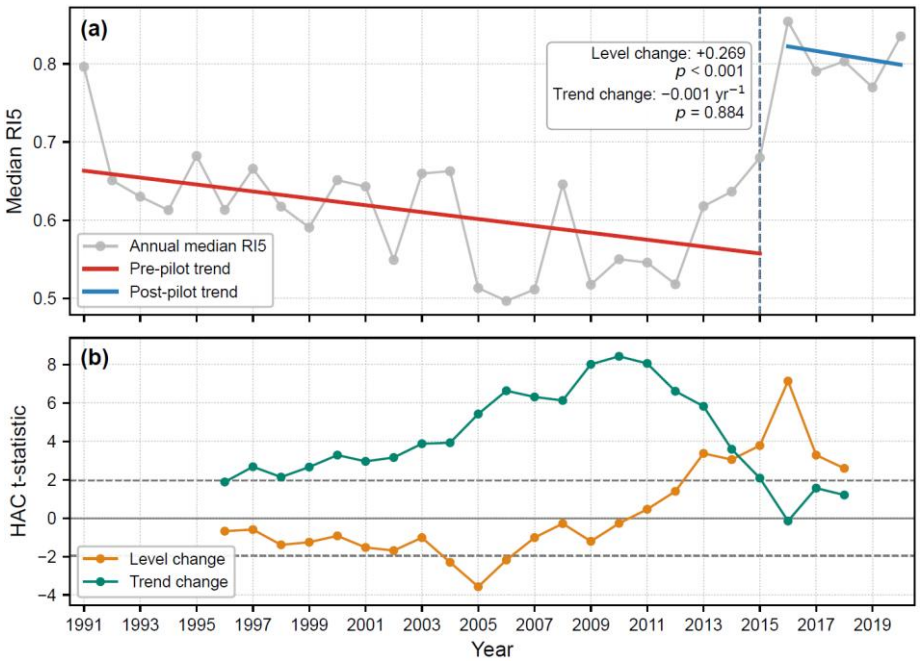


Figure 6. Interrupted time-series analysis of annual median five-year spectral recovery (RI5). (**a**) Annual median RI5 and fitted pre- and post-pilot trends, with the vertical dashed line indicating the initiation of the Wuyishan National Park pilot in 2015. Inference for level and trend changes used Newey–West heteroskedasticity- and autocorrelation-consistent standard errors. (**b**) Rolling ITSA showing HAC-adjusted t-statistics for level and trend changes across candidate intervention years. Dashed horizontal lines indicate ±1.96 reference values.

3.2. Recovery Timing and R80 Attainment

Of the 37,091 post-disturbance recovery trajectories, 36,078 had at least one complete post-disturbance year available for recovery-timing analysis. By the end of 2025, 28,174 pixels (78.1%) had attained R80, whereas 7904 pixels (21.9%) remained right-censored. Among pixels with observed R80 attainment, Y2R80 ranged from 1 to 34 years, with a mean of 8.8 years, a median of 7 years, and an interquartile range of 4–11 years (Figure 7a). The distribution peaked at 4 years, when 16.8% of attained pixels first reached R80, and the frequency of first attainment generally declined thereafter, forming a long right tail.

Kaplan–Meier estimation was applied to incorporate right-censored trajectories for pixels that had not attained R80 by the end of their observation period. The cumulative probability crossed 0.5 at 9 years, yielding a Kaplan–Meier median time to first spectral R80 attainment of 9 years (95% patch-bootstrap CI: 8–9 years). The median remained unchanged when disturbances ending after 2010, 2015, or 2020 were successively excluded, despite differences in recovery among disturbance-end-year cohorts. This was 2 years longer than the median derived from pixels with observed R80 attainment alone, reflecting the inclusion of pixels that had not yet reached R80 during their available follow-up. The number of pixels remaining at risk decreased progressively with time as pixels either attained R80 or reached the end of their observation period (Figure 7b). The fixed 8-year analysis provided a complementary comparison under equal follow-up duration. Among

the 34,216 pixels with eight complete post-disturbance years, 16,734 (48.9%) attained R80 within this interval. This fixed-window attainment rate was close to 50%, consistent with the Kaplan–Meier median estimate of 9 years.

Visual interpretation of 300 randomly sampled disturbed pixels was used to assess model-derived recovery timing. Among the 242 pixels for which at least one assessment identified R80 attainment, 211 (87.2%) showed agreement within ±3 years, with cases of inconsistent attainment status counted as disagreements. Among the 230 pixels for which both assessments identified R80 attainment, the mean absolute difference was 1.43 years.

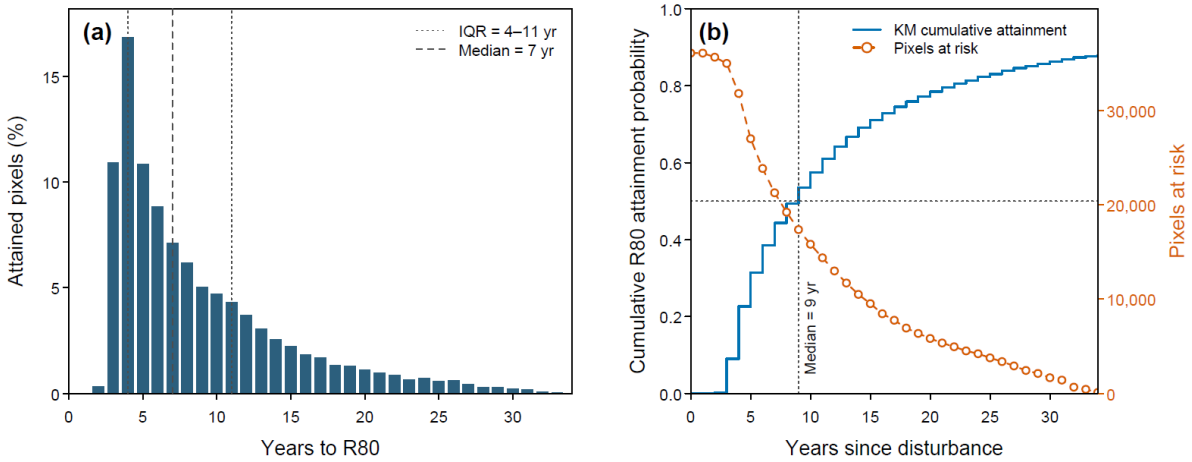


Figure 7. Post-disturbance timing and cumulative attainment of the spectral R80 threshold. (**a**) Distribution of Y2R80 among pixels that attained R80 by the end of 2025; vertical reference lines indicate the interquartile range (4–11 years) and median (7 years). (**b**) Kaplan–Meier estimate of cumulative R80 attainment; reference lines indicate a probability of 0.5 and the corresponding median recovery time of 9 years (95% patch-bootstrap CI: 8–9 years). The secondary y-axis shows the number of pixels remaining at risk.

3.3. Factors Associated with Recovery

The final GAMM analysis included 34,842 pixels from 3953 disturbance patches after excluding two extreme RI5 observations. Under five-fold patch-grouped cross-validation, pooled out-of-fold R^2 increased from 0.029 in M1 (disturbance characteristics) to 0.054 in M2 after adding patch characteristics and 0.078 in M3 with terrain variables (Table 1). Adding landscape context in M4 (R^2 = 0.088, ΔR^2 = 0.010) and climate variables in M5 (R^2 = 0.088, ΔR^2 = 0.0001) yielded smaller increments whose 95% confidence intervals included zero, while out-of-fold RMSE decreased overall from 0.312 in M1 to 0.303 in M5. For comparison, the full-data M5 model including patch-level random intercepts yielded a conditional in-sample R^2 of 0.518 and an RMSE of 0.220.

Table 1. Predictive performance of nested GAMMs and incremental contributions of explanatory-variable groups.

Model	Added Variable Group	OOF R^2	OOF RMSE	ΔR^2 (95% CI)
M1	Disturbance characteristics	0.029	0.312	—
M2	Patch characteristics	0.054	0.308	0.024 (0.008–0.040)
M3	Terrain	0.078	0.304	0.024 (0.005–0.041)
M4	Landscape context	0.088	0.303	0.010 (−0.0003–0.020)
M5	Climate	0.088	0.303	0.0001 (−0.017–0.015)

In the final M5 model, 13 of the 15 smooth terms were statistically significant (p < 0.001), whereas slope (p = 0.088) and distance to villages (p = 0.178) were not (Table 2;

Figure 8). RNDM exhibited the largest partial-effect range (0.341), followed by elevation (0.309), five-year mean temperature (0.252), and extreme VPD days (0.190).

Table 2. Smooth-term statistics for the GAMM of five-year spectral recovery (RI5).

Category	Variable	edf	F	*p*
Disturbance characteristics	RNDM	8.97	250.16	<0.001
	Duration	2.88	102.72	<0.001
Patch characteristics	Patch area	3.84	17.09	<0.001
	Patch shape index	2.67	9.49	<0.001
	Distance to patch edge	3.04	59.51	<0.001
Terrain	Elevation	7.08	22.47	<0.001
	Slope	2.71	1.93	0.088
Landscape context	Distance to park boundary	5.03	7.90	<0.001
	Distance to road	7.51	4.72	<0.001
	Distance to river	2.94	8.26	<0.001
	Distance to village	4.09	1.65	0.178
Climate	Cumulative precipitation	5.39	7.31	<0.001
	Mean temperature	8.24	19.61	<0.001
	Mean soil moisture	7.97	3.82	<0.001
	Extreme VPD days	8.75	26.96	<0.001

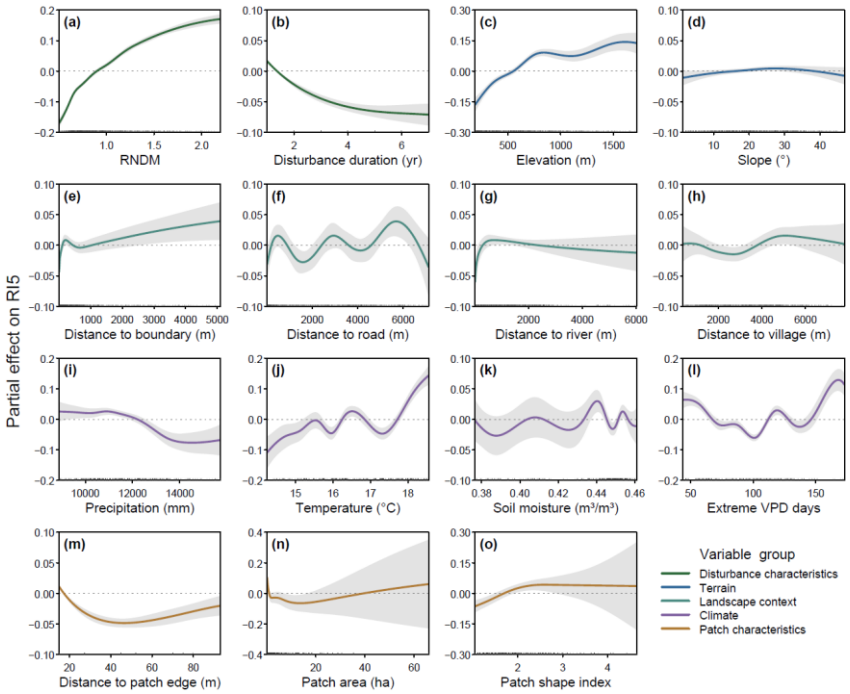


Figure 8. Adjusted GAMM relationships between five-year spectral recovery (RI5) and 15 explanatory variables representing disturbance characteristics (**a**,**b**), terrain (**c**,**d**), landscape context (**e**–**h**), climate (**i**–**l**), and patch characteristics (**m**–**o**). Colored lines show centered smooth partial effects for each variable group, shaded bands indicate 95% confidence intervals, dashed horizontal lines mark zero effect, and rug marks show predictor distributions. Y-axis ranges differ among panels to facilitate visualization of response shapes and uncertainty.

RI5 increased with RNDM and decreased with disturbance duration, with the steepest decline occurring over the first 4–5 years. Elevation exhibited a varying response across its range, while slope showed only a weak association. Among landscape variables, RI5 generally increased with distance from the park boundary. The response to road distance fluctuated, while RI5 increased with distance from rivers before approaching a relatively stable

level. Distance to villages showed no statistically significant association. All four climate variables exhibited significant smooth relationships with RI5, with larger partial-effect ranges for temperature and extreme VPD days than for precipitation and soil moisture. Among patch characteristics, RI5 decreased with distance from the patch edge to approximately 40–50 m before increasing slightly. RI5 reached a minimum at patch areas of approximately 10–15 ha, followed by an increase toward larger patches, although uncertainty widened. RI5 increased with patch shape index at lower values before approaching a plateau.

3.4. Sensitivity and Robustness Analyses

Recovery estimates varied with spectral-variable choice (Table 3). The adaptive approach yielded a median RI5 of 0.627 and an eight-year R80 attainment rate of 48.9%, compared with 0.331 and 18.2% for B5, 0.460 and 29.6% for B7, 0.500 and 40.0% for NBR, 0.422 and 25.4% for TCW, and 0.646 and 55.0% for NDFI, respectively. Among the 300 visually interpreted pixels, 138 had valid corresponding disturbance events across all five spectral variables and were retained for the cross-variable comparison. Kaplan–Meier estimates of eight-year R80 attainment for this subset ranged from 13.9% for B5 to 50.4% for NDFI. The NDFI–B5 difference was 36.5 percentage points (95% patch-bootstrap CI: 27.8–45.7 percentage points). Adaptive selection improved composite agreement with visual interpretation by 2.3–13.1 percentage points relative to fixed-variable approaches, although the differences were less conclusive for B5 and TCW.

On the common sample used for the spectral-variable sensitivity comparison, the adjusted end-to-end patch-edge contrast remained negative under all four formulations, although its magnitude differed among the adaptive, NBR, TCW, and NDFI approaches. Recovery timing also varied systematically with the selected threshold (Table 3). The Kaplan–Meier median time to first threshold attainment increased from 6 years for R70 to 9 years for R80 and 13 years for R90, with corresponding 95% patch-bootstrap confidence intervals of 6–7, 8–9, and 12–13 years, respectively. Within the common complete 8-year cohort, attainment declined from 61.9% for R70 to 48.9% for R80 and 35.8% for R90. Fixed-window R80 attainment increased from 38.3% within 6 years to 48.9% within 8 years and 56.2% within 10 years. The corresponding analyses retained 96.0%, 94.8%, and 91.7% of the recovery-timing population, respectively.

Table 3. Sensitivity of recovery estimates to spectral-variable choice, recovery threshold, and follow-up duration.

Sensitivity Component	Specification	Median RI5	KM Median Time (95% CI), yr	Fixed-Window Attainment (%)	Population Retained (%)
Spectral-variable choice	Adaptive approach	0.627	–	48.9	–
	B5	0.331	–	18.2	–
	B7	0.460	–	29.6	–
	NBR	0.500	–	40.0	–
	TCW	0.422	–	25.4	–
	NDFI	0.646	–	55.0	–
Recovery threshold	R70	–	6 (6–7)	61.9	–
	R80	–	9 (8–9)	48.9	–
	R90	–	13 (12–13)	35.8	–
Follow-up duration	6 yr	–	–	38.3	96.0
	8 yr	–	–	48.9	94.8
	10 yr	–	–	56.2	91.7

Excluding the upper and lower 0.5% of RI5 observations had little effect on the six smooth relationships examined in paired auxiliary models (Spearman's ρ = 0.991–1.000). Accounting for the patch-level random intercept reduced neighboring residual correlations from 0.494 to 0.186 at 30 m, 0.358 to 0.061 at 60 m, and 0.294 to 0.029 at 90 m. Conditional residual correlations were close to zero at 150 m (0.000) and 300 m (−0.037), although some spatial dependence remained at shorter distances.

Sensitivity to RNDM adjustment differed among predictors. Smooth-response shapes remained highly similar for 12 of the 14 remaining predictors (Spearman's ρ = 0.915–1.000), including disturbance duration, elevation, slope, distances to the park boundary, roads and rivers, patch area and shape, and all four climate variables. Distance to villages showed lower similarity (ρ = 0.880), although its association remained weak and statistically unsupported in the full GAMM. In contrast, the patch-edge relationship was strongly sensitive to RNDM adjustment (ρ = 0.098), with its modeled end-to-end contrast shifting from −0.031 in the full model to +0.032 after RNDM was excluded.

Overall, recovery estimates varied with spectral-variable choice, recovery threshold, and follow-up duration. Most modeled predictor–RI5 relationships remained similar after excluding extreme RI5 observations and adjusting for RNDM, whereas the patch-edge relationship was particularly sensitive to RNDM adjustment.

4. Discussion

4.1. Post-2015 Disturbance and Recovery Patterns

Post-disturbance recovery was spatially heterogeneous across Wuyishan National Park, while a distinct temporal shift emerged around the national park pilot. Annual median RI5 was generally higher after 2015, and ITSA characterized this temporal change primarily as an upward level shift rather than a change in the subsequent trend. The post-2015 difference also persisted when historical pixels were matched on measured disturbance, patch, terrain, and landscape characteristics. Whereas our previous study documented a decline in forest disturbance after 2015 [28], the present analysis shows that this period also coincided with higher five-year spectral recovery among disturbed pixels. At the national scale, assessments of China's pilot national parks have likewise reported reduced human disturbance and improved management effectiveness following protected-area integration and management reforms [32]. Changes in disturbance composition may also have contributed to this pattern. A post-2015 decline in persistent forest conversion could have increased the proportion of disturbances capable of subsequent vegetation recovery. Evidence from our previous study supports this interpretation. Tea-plantation expansion was identified as an important form of permanent anthropogenic forest conversion in Wuyishan and declined following the national park pilot [28]. This interpretation remains inferential because disturbance causes were not classified in the present study. These findings indicate that disturbance occurrence and post-disturbance recovery provide complementary information for assessing forest dynamics in protected areas.

4.2. Recovery Extends Beyond Short Monitoring Windows

Five years after disturbance, spectral recovery remained incomplete across much of the disturbed area. When right-censored trajectories were incorporated, the median time to first R80 attainment was 9 years, compared with 7 years among pixels that had already attained R80. This difference indicates that analyses restricted to observed attainments preferentially represent faster-recovering events and can underestimate recovery time. The 9-year estimate is consistent with Landsat-based studies showing that spectral recovery often extends beyond several years and varies markedly among disturbance types and regions [7,17].

Recovery time increased with increasingly stringent thresholds, indicating that it is an operational estimate tied to the selected recovery criterion rather than a fixed ecological property. Although recovery estimates varied among spectral indicators, visual interpretation of randomly sampled disturbed pixels generally supported the adaptive approach, which also showed higher composite agreement than fixed-variable alternatives in paired comparisons, albeit with less conclusive differences for B5 and TCW. This suggests that adaptive selection can accommodate pixel-level variation in spectral responses, while absolute recovery estimates remain dependent on spectral-variable choice. The use of R80 is supported by previous Landsat studies. White et al. [20], for example, found that an 80% NBR recovery threshold corresponded well with LiDAR-derived canopy height and cover in regenerating forests. Nevertheless, spectral recovery may precede the restoration of forest structure [21]. The 9-year median should therefore be interpreted as the time to first spectral R80 attainment, rather than the complete recovery of forest structure, composition, or ecological function.

Short observation windows can capture early vegetation return but may miss substantial portions of the recovery trajectory. Multi-year to decadal monitoring is therefore needed to distinguish disturbances that continue to recover from those that remain below their pre-disturbance spectral condition after sufficient follow-up. Persistent low-recovery areas can then be prioritized for field assessment, while decisions on active restoration should incorporate structural, compositional, and site-level ecological evidence rather than rely on spectral recovery alone.

4.3. Factors Associated with Recovery Heterogeneity

Disturbance duration was negatively associated with RI5, with the strongest decline occurring during the earlier part of the fitted spectral decline. In the LandTrendr framework, duration represents the length of the fitted spectral decline rather than a specific disturbance agent, and longer durations may reflect more gradual or persistent disturbance processes [8]. Previous studies have linked disturbance characteristics to recovery trajectories [7,17], while variation in five-year recovery among disturbance types has been reported in Northeast China [23]. RNDM also showed a strong positive association with RI5, but this should not be interpreted as evidence that more severe disturbances recover faster, because both metrics incorporate disturbance spectral amplitude.

RI5 decreased as patch area expanded from very small sizes, reaching a minimum at approximately 10–15 ha before increasing in larger patches, although uncertainty widened. Patch geometry may influence regeneration through surviving vegetation, propagule availability, and the spatial arrangement of disturbed interiors [40]. RI5 also increased with patch shape index at lower values. The association with patch-edge distance changed markedly when RNDM was excluded from the model, indicating sensitivity to model specification.

Elevation showed a complex relationship with RI5, while slope showed no statistically significant association. Among landscape variables, RI5 was lower near rivers and increased with distance, although this association may reflect correlated site conditions rather than a direct effect of river proximity. The modeled relationships with park-boundary and road distances also varied across their ranges, without clear evidence of a single underlying mechanism.

Previous research in southern Chinese plantation forests reported associations between short-term recovery and climatic and topographic factors [22]. All four climate variables showed statistically significant smooth associations with RI5, but their addition did not improve out-of-patch prediction. More broadly, adding patch characteristics and terrain improved out-of-patch prediction, whereas adding landscape and climate variables provided little further improvement.

4.4. Management Implications and Limitations

While disturbance maps identify where forest change occurred, integrating them with recovery trajectories further distinguishes areas undergoing continued recovery from those remaining at low recovery levels. Disturbance duration and patch characteristics may further inform monitoring priorities. However, the modest out-of-patch predictive performance of the GAMM limits its use for precise predictions at individual pixels or patches. The modeled relationships are more appropriate for characterizing recovery heterogeneity and supporting broad-scale screening, alongside subsequent observations and field assessments.

Several limitations remain. First, spectral recovery does not directly measure forest structure, species composition, or ecosystem function, and the 30 m Landsat resolution may obscure fine-scale variation. Second, the coarser resolution of the climate data may not capture local climatic differences in this mountainous landscape, potentially limiting their additional predictive contribution. Moreover, the climate variables describe conditions during the same five-year period used to calculate RI5 rather than conditions known at the disturbance endpoint. Finally, disturbance types were not distinguished because consistent historical reference data on disturbance agents were unavailable and archival high-resolution imagery was sparse and temporally discontinuous. The results therefore characterize broad-scale recovery patterns rather than type-specific trajectories.

5. Conclusions

This study characterized the magnitude, timing, and spatial heterogeneity of post-disturbance forest recovery in Wuyishan National Park using Landsat time series from 1990 to 2025. The adaptive spectral-variable selection approach was generally supported by visual interpretation, although recovery estimates varied among spectral indicators and recovery thresholds. Five years after disturbance, median RI5 was 0.627, and 29.5% of disturbed pixels had recovered at least 80% of the initial spectral loss. After accounting for right censoring, the median time to first R80 attainment was 9 years. Annual median RI5 showed a marked upward level shift from 2016 onward, coinciding with the national park pilot. Longer disturbance duration, intermediate-sized patches, and proximity to rivers were associated with lower RI5. Patch characteristics and terrain improved out-of-patch prediction, whereas adding landscape and climate variables yielded little further improvement. By integrating adaptive spectral assessment, recovery-time estimation that accounts for right censoring, and patch-grouped prediction evaluation, this study extends disturbance-based monitoring beyond mapping forest change to characterizing recovery trajectories and distinguishing factors associated with recovery from those that improve its prediction across disturbance patches.

Author Contributions: Conceptualization, H.L. and L.Z.; methodology, H.L. and F.Z.; validation, H.M. and Y.X.; formal analysis, H.L. and Y.X.; investigation, Y.X.; resources, F.Z.; data curation, H.L. and H.M.; writing—original draft preparation, H.L.; writing—review and editing, F.Z., H.M. and L.Z.; visualization, H.L.; supervision, L.Z.; project administration, F.Z. and L.Z. All authors have read and agreed to the published version of the manuscript.

Funding: This research received no external funding.

Data Availability Statement: The Landsat imagery and ancillary datasets used in this study are available from the public sources described in the article. The classification code and dataset used for the disturbance classification are publicly available on Zenodo (DOI: 10.5281/zenodo.23103874).

Conflicts of Interest: The authors declare no conflicts of interest.

References

1. Geldmann, J.; Barnes, M.; Coad, L.; Craigie, I.D.; Hockings, M.; Burgess, N.D. Effectiveness of Terrestrial Protected Areas in Reducing Habitat Loss and Population Declines. *Biol. Conserv.* **2013**, *161*, 230–238. https://doi.org/10.1016/j.biocon.2013.02.018.
2. Geldmann, J.; Manica, A.; Burgess, N.D.; Coad, L.; Balmford, A. A Global-Level Assessment of the Effectiveness of Protected Areas at Resisting Anthropogenic Pressures. *Proc. Natl. Acad. Sci. USA* **2019**, *116*, 23209–23215. https://doi.org/10.1073/pnas.1908221116.
3. Jones, K.R.; Venter, O.; Fuller, R.A.; Allan, J.R.; Maxwell, S.L.; Negret, P.J.; Watson, J.E.M. One-Third of Global Protected Land Is under Intense Human Pressure. *Science* **2018**, *360*, 788–791. https://doi.org/10.1126/science.aap9565.
4. Nagendra, H.; Lucas, R.; Honrado, J.P.; Jongman, R.H.G.; Tarantino, C.; Adamo, M.; Mairota, P. Remote Sensing for Conservation Monitoring: Assessing Protected Areas, Habitat Extent, Habitat Condition, Species Diversity, and Threats. *Ecol. Indic.* **2013**, *33*, 45–59. https://doi.org/10.1016/j.ecolind.2012.09.014.
5. Willis, K.S. Remote Sensing Change Detection for Ecological Monitoring in United States Protected Areas. *Biol. Conserv.* **2015**, *182*, 233–242. https://doi.org/10.1016/j.biocon.2014.12.006.
6. Ibáñez, I.; Acharya, K.; Juno, E.; Karounos, C.; Lee, B.R.; McCollum, C.; Schaffer-Morrison, S.; Tourville, J. Forest Resilience under Global Environmental Change: Do We Have the Information We Need? A Systematic Review. *PLoS ONE* **2019**, *14*, e0222207. https://doi.org/10.1371/journal.pone.0222207.
7. Senf, C.; Seidl, R. Post-disturbance Canopy Recovery and the Resilience of Europe's Forests. *Glob. Ecol. Biogeogr.* **2022**, *31*, 25–36. https://doi.org/10.1111/geb.13406.
8. Kennedy, R.E.; Yang, Z.; Cohen, W.B. Detecting Trends in Forest Disturbance and Recovery Using Yearly Landsat Time Series: 1. LandTrendr—Temporal Segmentation Algorithms. *Remote Sens. Environ.* **2010**, *114*, 2897–2910. https://doi.org/10.1016/j.rse.2010.07.008.
9. DeVries, B.; Decuyper, M.; Verbesselt, J.; Zeileis, A.; Herold, M.; Joseph, S. Tracking Disturbance-Regrowth Dynamics in Tropical Forests Using Structural Change Detection and Landsat Time Series. *Remote Sens. Environ.* **2015**, *169*, 320–334. https://doi.org/10.1016/j.rse.2015.08.020.
10. Wulder, M.A.; Masek, J.G.; Cohen, W.B.; Loveland, T.R.; Woodcock, C.E. Opening the Archive: How Free Data Has Enabled the Science and Monitoring Promise of Landsat. *Remote Sens. Environ.* **2012**, *122*, 2–10. https://doi.org/10.1016/j.rse.2012.01.010.
11. Zhang, L.; Zhang, S.; Rehman, A.U.R.; Wang, S.; Sun, X.; Liu, Y.; Tong, Q. A Revolutionary Multi-Dimensional Data Format for Remote Sensing. *Innov.* **2025**, *6*, 100950. https://doi.org/10.1016/j.xinn.2025.100950.
12. Zhang, L.; Wang, S.; Liu, H.; Lin, Y.; Wang, J.; Zhu, M.; Gao, L.; Tong, Q. From Spectrum to Spectrotemporal: Research on Time Series Change Detection of Remote Sensing. *Geomat. Inf. Sci. Wuhan Univ.* **2021**, *46*, 451–468. https://doi.org/10.13203/j.whugis20200666.
13. Kennedy, R.E.; Yang, Z.; Cohen, W.B.; Pfaff, E.; Braaten, J.; Nelson, P. Spatial and Temporal Patterns of Forest Disturbance and Regrowth within the Area of the Northwest Forest Plan. *Remote Sens. Environ.* **2012**, *122*, 117–133. https://doi.org/10.1016/j.rse.2011.09.024.
14. White, J.C.; Wulder, M.A.; Hermosilla, T.; Coops, N.C.; Hobart, G.W. A Nationwide Annual Characterization of 25 Years of Forest Disturbance and Recovery for Canada Using Landsat Time Series. *Remote Sens. Environ.* **2017**, *194*, 303–321. https://doi.org/10.1016/j.rse.2017.03.035.
15. Hird, J.N.; Kariyeva, J.; McDermid, G.J. Satellite Time Series and Google Earth Engine Democratize the Process of Forest-Recovery Monitoring over Large Areas. *Remote Sens.* **2021**, *13*, 4745. https://doi.org/10.3390/rs13234745.
16. Senf, C.; Müller, J.; Seidl, R. Post-Disturbance Recovery of Forest Cover and Tree Height Differ with Management in Central Europe. *Landsc. Ecol* **2019**, *34*, 2837–2850. https://doi.org/10.1007/s10980-019-00921-9.
17. White, J.C.; Hermosilla, T.; Wulder, M.A.; Coops, N.C. Mapping, Validating, and Interpreting Spatio-Temporal Trends in Post-Disturbance Forest Recovery. *Remote Sens. Environ.* **2022**, *271*, 112904. https://doi.org/10.1016/j.rse.2022.112904.
18. Frazier, R.J.; Coops, N.C.; Wulder, M.A.; Hermosilla, T.; White, J.C. Analyzing Spatial and Temporal Variability in Short-Term Rates of Post-Fire Vegetation Return from Landsat Time Series. *Remote Sens. Environ.* **2018**, *205*, 32–45. https://doi.org/10.1016/j.rse.2017.11.007.
19. Hermosilla, T.; Wulder, M.A.; White, J.C.; Coops, N.C. Prevalence of Multiple Forest Disturbances and Impact on Vegetation Regrowth from Interannual Landsat Time Series (1985–2015). *Remote Sens. Environ.* **2019**, *233*, 111403. https://doi.org/10.1016/j.rse.2019.111403.
20. White, J.C.; Saarinen, N.; Kankare, V.; Wulder, M.A.; Hermosilla, T.; Coops, N.C.; Pickell, P.D.; Holopainen, M.; Hyyppä, J.; Vastaranta, M. Confirmation of Post-Harvest Spectral Recovery from Landsat Time Series Using Measures of Forest Cover and Height Derived from Airborne Laser Scanning Data. *Remote Sens. Environ.* **2018**, *216*, 262–275. https://doi.org/10.1016/j.rse.2018.07.004.

21. Mandl, L.; Viana-Soto, A.; Seidl, R.; Stritih, A.; Senf, C. Unmixing-Based Forest Recovery Indicators for Predicting Long-Term Recovery Success. *Remote Sens. Environ.* **2024**, *308*, 114194. https://doi.org/10.1016/j.rse.2024.114194.
22. Zhu, F.; Wang, H.; Li, M.; Diao, J.; Shen, W.; Zhang, Y.; Wu, H. Characterizing the Effects of Climate Change on Short-Term Post-Disturbance Forest Recovery in Southern China from Landsat Time-Series Observations (1988–2016). *Front. Earth Sci.* **2020**, *14*, 816–827. https://doi.org/10.1007/s11707-020-0820-6.
23. Yu, Y.; Liu, Z.; Wang, W.; Xu, W.; Lv, Q.; Li, K.; Guo, W.; Fang, L.; Zhang, Q.; Wu, Z.; et al. Disturbance Types Play a Key Role in Post-Disturbance Vegetation Recovery in Boreal Forests of Northeast China. *Ecol. Indic.* **2024**, *168*, 112745. https://doi.org/10.1016/j.ecolind.2024.112745.
24. Morfopoulou, I.; Kokkoris, I.P.; Mitsopoulos, I.; Mallinis, G. Remote Sensing of Vegetation Dynamics: A Systematic Review on Disturbances in Protected Areas. *Forests* **2026**, *17*, 853. https://doi.org/10.3390/f17070853.
25. Wu, Q.; Lee, C.K.F.; Wang, J.A.; Zhao, Y.; Song, G.; Maeda, E.E.; Su, Y.; Huete, A.; Hughes, A.C.; Wu, J. Improved Assessment of Post-Fire Recovery Trajectory of Forests in Amazon's Protected Areas. *Remote Sens. Environ.* **2025**, *326*, 114802. https://doi.org/10.1016/j.rse.2025.114802.
26. Wu, Y.; Zhang, W.; Wang, Y.; Zhao, S.; Tian, J.; Shi, J.; Yang, X.; Cui, P. Effects of Landscape Context on Bird Community in the Subtropical Evergreen Broad-Leaved Forest of Wuyishan National Park. *Animals* **2023**, *13*, 1294. https://doi.org/10.3390/ani13081294.
27. Fan, X.; Zang, Z.; Tang, J.; Zhao, L.; Xu, W.; Ouyang, Z. Ecological Integrity Assessment System for Wuyishan National Park. *Ecol. Indic.* **2025**, *178*, 113910. https://doi.org/10.1016/j.ecolind.2025.113910.
28. Liu, H.; Zhang, F.; Xie, Y.; Mu, H.; Luo, S.; Liu, T.; Zhang, L. Long-Term Spatiotemporal Dynamics of Forest Disturbances in Wuyishan National Park: Patterns, Drivers, and Conservation Insights. *Int. J. Appl. Earth Obs. Geoinf.* **2026**, *150*, 105343. https://doi.org/10.1016/j.jag.2026.105343.
29. Fan, M.; Liao, K.; Lu, D.; Li, D. Examining Vegetation Change and Associated Spatial Patterns in Wuyishan National Park at Different Protection Levels. *Remote Sens.* **2022**, *14*, 1712. https://doi.org/10.3390/rs14071712.
30. Fujian Provincial Department of Forestry; Jiangxi Provincial Department of Forestry; Wuyishan National Park Administration. *The Master Plan of Wuyishan National Park (2023–2030)*; National Forestry and Grassland Administration: Beijing, China, 2023. https://wysgjgy.fujian.gov.cn/zwgk/jcgh/202312/t20231214_6330883.htm
31. He, S.; Su, Y.; Wang, L.; Gallagher, L.; Cheng, H. Taking an Ecosystem Services Approach for a New National Park System in China. *Resour. Conserv. Recycl.* **2018**, *137*, 136–144. https://doi.org/10.1016/j.resconrec.2018.04.030.
32. Zang, Z.; Guo, Z.; Fan, X.; Han, M.; Du, A.; Xu, W.; Ouyang, Z. Assessing the Performance of the Pilot National Parks in China. *Ecol. Indic.* **2022**, *145*, 109699. https://doi.org/10.1016/j.ecolind.2022.109699.
33. Sheng, C.; Wang, Y.; Ye, S. Discussion on the National Park Management Mode under China's National Park System: A Case of Wuyishan National Park System Pilot Area. *Int. J. Geoheritage Parks* **2020**, *8*, 230–234. https://doi.org/10.1016/j.ijgeop.2020.11.004.
34. Liu, Z.; Wang, W.J.; Ballantyne, A.; He, H.S.; Wang, X.; Liu, S.; Ciais, P.; Wimberly, M.C.; Piao, S.; Yu, K.; et al. Forest Disturbance Decreased in China from 1986 to 2020 despite Regional Variations. *Commun Earth Env.* **2023**, *4*, 15. https://doi.org/10.1038/s43247-023-00676-x.
35. Kennedy, R.E.; Yang, Z.; Gorelick, N.; Braaten, J.; Cavalcante, L.; Cohen, W.B.; Healey, S. Implementation of the LandTrendr Algorithm on Google Earth Engine. *Remote Sens.* **2018**, *10*, 691. https://doi.org/10.3390/rs10050691.
36. Kaplan, E.L.; Meier, P. Nonparametric Estimation from Incomplete Observations. *J. Am. Stat. Assoc.* **1958**, *53*, 457–481. https://doi.org/10.1080/01621459.1958.10501452.
37. Washaya, P.; Potterf, M.; Modlinger, R.; Hüttnerová, T.; Melichová, Z.; Hlásny, T. Severely Disturbed Forests in Central Europe Retain Robust Recovery Capacity but Face Resilience Loss Due to Spatial Homogenization. *Landsc Ecol* **2025**, *41*, 9. https://doi.org/10.1007/s10980-025-02264-0.
38. Pickell, P.D.; Hermosilla, T.; Frazier, R.J.; Coops, N.C.; Wulder, M.A. Forest Recovery Trends Derived from Landsat Time Series for North American Boreal Forests. *Int. J. Remote Sens.* **2016**, *37*, 138–149. https://doi.org/10.1080/2150704X.2015.1126375.

39. Wood, S.N. *Generalized Additive Models: An Introduction with R*; 2nd ed.; Chapman and Hall/CRC: Boca Raton, FL, USA, 2017; ISBN 978-1-315-37027-9.
40. Seidl, R.; Turner, M.G. Post-Disturbance Reorganization of Forest Ecosystems in a Changing World. *Proc. Natl. Acad. Sci. USA* **2022**, *119*, e2202190119. https://doi.org/10.1073/pnas.2202190119.

Disclaimer/Publisher's Note: The statements, opinions and data contained in all publications are solely those of the individual author(s) and contributor(s) and not of MDPI and/or the editor(s). MDPI and/or the editor(s) disclaim responsibility for any injury to people or property resulting from any ideas, methods, instructions or products referred to in the content.